Nakamura Rumi (Orcid ID: 0000-0002-2620-9211)
Varsani Ali (Orcid ID: 0000-0003-1814-1568)
Genestreti Kevin, J (Orcid ID: 0000-0001-6890-2973)
Le Contel Olivier (Orcid ID: 0000-0003-2713-7966)
Nakamura Takuma (Orcid ID: 0000-0003-4550-2947)
Baumjohann Wolfgang (Orcid ID: 0000-0001-6271-0110)
Nagai Tsugunobu (Orcid ID: 0000-0002-3238-864X)
Artemyev Anton, V (Orcid ID: 0000-0001-8823-4474)
Birn Joachim (Orcid ID: 0000-0002-1496-4076)
Sergeev Victor, A. (Orcid ID: 0000-0002-4569-9631)
Ergun Robert, E (Orcid ID: 0000-0002-3096-8579)
Fuselier Stephen (Orcid ID: 0000-0003-4101-7901)
Gershman Daniel, J (Orcid ID: 0000-0003-1304-4769)
Giles Barbara, L. (Orcid ID: 0000-0001-8054-825X)
Khotyaintsev Yuri, V. (Orcid ID: 0000-0001-5550-3113)
Lindqvist Per-Arne (Orcid ID: 0000-0001-5617-9765)
Magnes Werner (Orcid ID: 0000-0003-0086-6288)
Mauk Barry, H. (Orcid ID: 0000-0001-9789-3797)
Petrukovich Anatoli (Orcid ID: 0000-0002-2117-9842)
Russell Christopher T. (Orcid ID: 0000-0003-1639-8298)
Strangeway Robert, J. (Orcid ID: 0000-0001-9839-1828)
Anderson Brian, J. (Orcid ID: 0000-0003-2543-0149)
Burch James, L (Orcid ID: 0000-0003-0452-8403)
Bromund Kenneth, R (Orcid ID: 0000-0003-0383-7845)
Cohen Ian, James (Orcid ID: 0000-0002-9163-6009)
Fischer David (Orcid ID: 0000-0002-8435-7220)
Jaynes Allison, N (Orcid ID: 0000-0002-1470-4266)
Kepko Laurence (Orcid ID: 0000-0002-4911-8208)
Le Guan (Orcid ID: 0000-0002-9504-5214)
Plaschke Ferdinand (Orcid ID: 0000-0002-5104-6282)
Reeves Geoffrey, D. (Orcid ID: 0000-0002-7985-8098)
Singer Howard, J. (Orcid ID: 0000-0002-5364-6505)
Slavin James, A. (Orcid ID: 0000-0002-9206-724X)
Torbert Roy, B. (Orcid ID: 0000-0001-7188-8690)
Turner Drew, L. (Orcid ID: 0000-0002-2425-7818)

Multi-scale currents observed by MMS in the flow braking region

Rumi Nakamura[1], Ali Varsani[1], Kevin J. Genestreti[1], Olivier Le Contel[2], Takuma Nakamura[1], Wolfgang Baumjohann[1], Tsugunobu Nagai[3], Anton Artemyev[4], Joachim Birn[5], Victor A. Sergeev[6], Sergey Apatenkov[6], Robert E Ergun[7], Stephen A. Fuselier[8], Daniel J. Gershman[9], Barbara J. Giles[9], Yuri V. Khotyaintsev[10], Per-Arne Lindqvist[11], Werner Magnes[1], Barry Mauk[12], Anatoli Petrukovich[13], Christopher T. Russell[4], Julia Stawarz[14], Robert J. Strangeway[4], Brian Anderson[12], James L. Burch[8], Ken R. Bromund[9], Ian Cohen[12], David Fischer[1], Allison Jaynes[7] Laurence Kepko[9], Guan Le[9], Ferdinand Plaschke[1], Geoff Reeves[15], Howard J. Singer[16], James A. Slavin[17], Roy B. Torbert[8,18], Drew L. Turner[19]

[1]Space Research Institute, Austrian Academy of Sciences, Graz, Austria.
[2] Laboratoire de Physique des Plasmas, CNRS/ Ecole polytechnique/UPMC Univ Paris 06/Univ. Paris-Sud/Observatoire de Paris, Paris, France

[3]Tokyo Institute of Technology, Tokyo, Japan.

[4] University of California, Los Angeles, USA.

This is the author manuscript accepted for publication and has undergone full peer review but has not been through the copyediting, typesetting, pagination and proofreading process, which may lead to differences between this version and the Version of Record. Please cite this article as doi: 10.1002/2017JA024686

[5]Space Science Institute, Boulder, USA.

[6]St. Petersburg State University, St. Petersburg, Russia.

[7]LASP, University of Colorado, Boulder, Colorado, USA.

[8]Southwest Research Institute, San Antonio, USA.

[9]NASA, Goddard Space Flight Center, Greenbelt, USA.

[10]Swedish Institute of Space Physics, Uppsala, Sweden.

[11]Royal Institute of Technology, Stockholm, Sweden.

[12]Applied Physics Laboratory, Johns Hopkins University, Laurel, USA.

[13]Space Research Institute (IKI), RAS, Moscow, Russia.

[14]Department of Physics, Imperial College London, London, UK.

[15] LANL, CSES, New Mexico, USA.

[16] NOAA Space Weather Prediction Center, Boulder, Colorado, USA.

[17]Department of Climate and Space Sciences and Engineering, University of Michigan, Ann Arbor, USA.

[18] Univ New Hampshire, Inst Study Earth Oceans & Space, Durham, USA.

[19]Space Sciences Department, Aerospace Corporation, Los Angeles, USA.

Corresponding author: Rumi Nakamura (rumi.nakamura@oeaw.ac.at)

Key Points:

- Multi-scale field-aligned currents in the boundary of the expanding plasma sheet during plasma jet braking intervals are resolved.
- Intense Hall-current layers are found at the inner boundary of the hot Earthward streaming ion jets and flow shear regions.
- Both plasma jet diversion and Hall-effects from reconnection region contribute to the structure of the substorm wedge currents.

Abstract

We present characteristics of current layers in the off-equatorial near-Earth plasma sheet boundary observed with high time-resolution measurements from the Magnetospheric Multiscale (MMS) mission during an intense substorm associated with multiple dipolarizations. The four MMS spacecraft, separated by distances of about 50 km, were located in the southern hemisphere in the dusk portion of a substorm current wedge. They observed fast flow disturbances (up to about 500 km/s), most intense in the dawn-dusk direction. Field-aligned currents were observed initially within the expanding plasma sheet, where the flow and field disturbances showed the distinct pattern expected in the braking region of localized flows. Subsequently, intense thin field-aligned currents layers were detected at the inner boundary of equatorward moving flux tubes together with Earthward streaming hot ions. Intense Hall-current layers were found adjacent to the field-aligned currents. In particular, we found a Hall-current structure in the vicinity of the Earthward streaming ion jet, that consisted of mixed ion components, i.e., hot unmagnetized ions, cold E x B drifting ions, and magnetized electrons. Our observations show that both the near-Earth plasma jet diversion and the thin Hall-current layers formed around the reconnection jet boundary are the sites where diversion of the perpendicular currents take place that contribute to the observed field-aligned current pattern as predicted by simulations of reconnection jets. Hence, multiscale structure of flow braking is preserved in the field-aligned currents in the off-equatorial plasma sheet and is also translated to ionosphere to become a part of the substorm field-aligned current system.

1 Introduction

The most dramatic energy release in the near-Earth magnetotail is considered to be driven by the near-Earth magnetic reconnection-associated flows, called bursty bulk flows (BBFs), and electromagnetic disturbances propagating Earthward and interacting with plasmas in the near-Earth dipolar region. In particular, during substorms these disturbances lead to drastic changes in the magnetospheric configuration such as thinning and expansion of the plasma sheet, magnetic field dipolarization, and energetic particle injection. Enhanced coupling to the ionosphere results in strong currents, e.g., auroral electrojets, field-aligned currents (FACs), and auroral precipitations. The large-scale current system during the substorm expansion phase, called the substorm current wedge (SCW) [McPherron et al., 1973], consists of a net FAC toward the magnetosphere out from the ionosphere (upward FAC) at the western edge and into the ionosphere at the eastern edge of the auroral activity, which is connected by a westward horizontal current in the ionosphere. A similar field-aligned current pattern was also identified during localized magnetospheric disturbances such as pseudobreakups [Nakamura et al., 2001; Palin et al., 2015] as well as during BBFs [e.g., Henderson et al., 1998; Nakamura et al., 2001].

The occurrence frequency of Earthward BBFs or the rapid flux transport rate (enhanced dawn-to-dusk electric field) significantly drops inward of 10-15 R_E [e.g., Schödel et al., 2001], called the flow braking region, where significant energy dissipation and current disruption (unloading) processes take place [e.g. Sergeev et al., 2012, and references therein]. It is the flow-braking region where larger E_Y than in the midtail region was detected [Tu et al., 2000, Liu et al., 2014; Schmid et al., 2016], indicating that the flux transport rate itself may increase before the flows brake. A large dawn-to-dusk electric field is obtained also in MHD simulations due to the induced electric field in the flow-braking region [Birn and Hesse, 1996; Birn et al., 2011]. Vortex flows, oscillatory behavior of the flows [e.g., Panov et al., 2013], and small-scale current sheet processes that break the frozen-in condition have been reported in this region [e.g., Lui, 2013], suggesting that the flow braking involves dynamic multi-scale processes.

On August 10, 2016 an intense (AL ~ -1000 nT) substorm was initiated at 09:57 UT when multiple spacecraft were distributed at radial distances between 4 and 15 R_E in the night-side magnetosphere. The four spacecraft of the Magnetospheric Multiscale (MMS) were located in the southern hemisphere outer plasma sheet and observed fast flow disturbances associated with multiple dipolarizations. Nakamura et al., [2017] (hereafter referred to as Nak17) studied the large-scale evolution of the current wedge based on the multiple spacecraft in the night-side magnetosphere and ground-based observations. Several intense field-aligned current layers were identified from MMS observations. Based on the analysis of the flows and motion of these FACs in comparison with other spacecraft and MHD simulations [Birn and Hesse, 2014], it was concluded that MMS encountered a FAC system at the high-latitude side of the near-Earth flow-braking region. These observations show that the processes of Earthward flow braking as well as accumulated magnetic flux evolving tailward, which has

been detected in the center of the plasma sheet [Nakamura et al., 2009], can be also detected at the boundary region of the near-Earth plasma sheet. In this paper we study the characteristics of each FAC layer as well as the perpendicular currents observed by MMS. Using high-resolution ion and electron data, particle population responsible for the currents is examined to understand the physical processes of these active plasma boundaries.

2 Overview of the event

On August 10, 2016, MMS crossed the near-Earth tail region when an intense substorm with multiple intensifications in the electrojet (Figure 1) commenced at 09:57 UT. The Bz component of the magnetic field (panel a), obtained from Geostationary Operational Environmental Satellites (GOES) 14-15 [Singer et al., 1996], MMS [Russell et al., 2014], and Geotail [Kokubun et al., 1994], show that multiple dipolarizations were observed by these spacecraft associated with an energetic particle injection (panel b) and an intense electrojet enhancement (panel c). Based on the analysis of the magnetic field disturbances at GOES 14, 15, MMS, Geotail, and ground-based magnetic field observations, it was shown that a substorm current wedge developed in the nightside region. MMS was located at the dusk part of the substorm current wedge (Nak17), close to the geosynchronous satellites, GOES 15 and LANL01A. The projected magnetic field lines from the T89 model [Tsyganenko, 1989] (panel 1d) show that MMS was on a field line that crosses the equator about 3 R_E tailward of LANL-01A. Since MMS was in the near-Earth region, we will use the following coordinate systems in reference to the Earth's dipole, i.e., the solar magnetic (SM) system or VDH coordinate system (explained below). The direction of the VDH axis for MMS, projected on the GSM equatorial plane is given in panel d. The location of the four MMS spacecraft in the SM system was (X_{SM}, Y_{SM}, Z_{SM}) = (-6.7, 2.4, -2.2)R_E in the premidnight (22.7MLT) region. The spacecraft separation was about 50 km, as shown in Figures 1e and 1f. In this paper, we examine the characteristics of the field-aligned current between 10:01 and 10:04 UT (the time interval indicated by the solid line) during the main part of the substorm expansion phase. During this time MMS was located at the western edge of a localized SCW, obtained based on analysis of low-altitude ground based data and disturbances of magnetic field data from GOES and Geotail (NAK17).

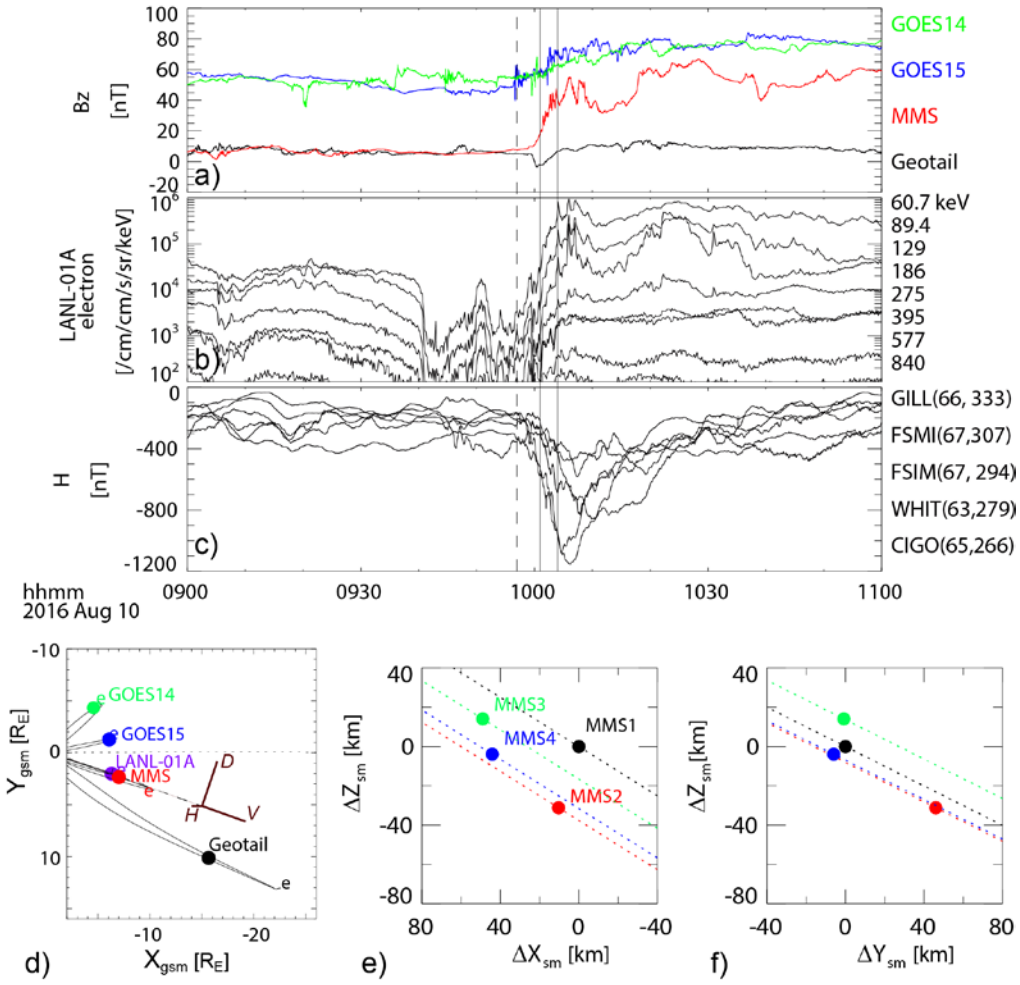

Figure 1. Overview of the August 10, 2016, 0957 UT substorm. (a) Bz component of the magnetic field obtained from GOES 14 (green), GOES 15 (blue), MMS (red), and Geotail (black); (b) Electron differential flux from LANL-01A; (c) Horizontal component of the geomagnetic field from ground stations; (d) location of the different spacecraft in the equatorial plane. Relative location of MMS spacecraft in (e) X-Z and (f) Y-Z planes. The dashed line in (a-c) shows the 09:57 UT substorm onset and the solid lines indicate 10:01 and 10:04 UT, which is the time interval of interest in this study. The curves drawn in (d) are the projected magnetic field lines from T89 model and equatorial location is marked with "e". Projected direction of the axis of the VDH coordinate system for MMS is given also in (d). The dotted lines in panels (e-f) show the satellite trajectories.

Figure 2 shows the plasma and magnetic observations from MMS between 10:01 UT and 10:04 UT. Electron and ion energy spectra from the MMS Energetic Ion Spectrometer (EIS) [Mauk et al. 2014] and the Fast Plasma Instruments (FPI) [Pollock, 2016] are shown in Figures 2a and 2b. The electron energy spectra is a combined product from the MMS1 EIS instrument for energy >25 keV and from the MMS3 FPI instrument for energy <25 keV (panel 2). To enhance the visibility of the high-energy part, the EIS electron energy flux is multiplied by 2.75. The ion energy spectrum shown in panel b is from MMS3 and is a composite of the proton data from EIS for higher energies (>30 keV) and ion data from FPI for lower energies (<30 keV). For the FPI ion data, the background noise due to energetic

electrons is subtracted. Here we first obtained the background counts, which are expected to be energy independent and are assumed to be the counts from the lowest energy channels (five lowest, typically), where we expect no actual plasma to be measured. The average counts are calculated for these low-energy channels and then these constant counts are removed from all the energy channels for each data sampling (150ms). The distribution functions and moments are then calculated from the background-subtracted data. The electron temperature and ion and electron densities from FPI are shown in panels c and d. MMS was located in the outer plasma sheet until around 10:01:30 UT, then entered into a hotter and denser plasma sheet region, as can be seen in the plasma density and the electron temperature. The ion energy spectra show that significant ion population shift to the energy of EIS so that the latter contribution becomes important in particular for temperature (not shown).

The entry into the hotter plasma sheet is associated with multiple dipolarizations, as can be seen in the magnetic field data from the four MMS spacecraft shown in panels e-g. Here we used the VDH coordinate system, since it better represents the magnetic disturbance in a dipolar configuration at a local time away from the midnight region. H is the same as the Z component in the SM along the geomagnetic dipole axis and is positive northward. D is perpendicular to H and the radial direction, R, and is positive eastward. V closes the right-hand coordinate system and is positive in the radially outward direction. For this event, therefore, +V and +D directions at MMS location correspond to approximately $-X_{SM}$ and $-Y_{SM}$ directions with about 19° clockwise rotations viewed from the north. The coordinate system is convenient for this event, since the background field parallel to the current sheet is nearly aligned to the V direction. The overall decrease in B_V (panel e) and increase in B_H (g) indicate the change from a tail-like to a more dipolar configuration associated with the expansion of the plasma sheet. The main disturbances during these events are the step-like changes in the B_D component (f) due to field-aligned currents, which is also confirmed by the current profile (panel h). Jb_perp and Jb_para shown in panel h are currents perpendicular and parallel to the magnetic field and are deduced by applying the curlometer method [Chanteur et al., 1998] to the magnetic field data from the four MMS spacecraft. The four main sharp changes in B_D, corresponding to the intense FAC layers, are all accompanied by dipolarization fronts (B_H enhancements). The dashed lines mark the start of these events: (i) 10:01:22, (ii) 10:01:43 (iii) 10:02:41 and (iv) 10:03:01. The FAC during event (i) was anti-parallel to the magnetic field direction, i.e., currents are flowing into the ionosphere (downward FAC). The direction of the FACs of event (ii)-(iv) was parallel to the magnetic field, i.e., currents are flowing out from the ionosphere (upward FAC).

Figure 2i depicts the 1-sec averaged FPI ion flow data, showing that the FAC events are related to enhancements in the high-speed flows, mainly in the dawn-dusk direction. Event (i) corresponds to enhancements in dawnward (+Vd)/northward (+Vh) flow. The flow changed to duskward (-Vd) during event (ii), followed by an enhancement in Earthward flow(-Vv). Event (iii) is associated with enhancement in northward (equatorward) flow direction, while event (iv) is followed by enhancement in Earthward (-Vv) flow. Note that the velocity moment, which is calculated using FPI with its limited energy range (<30 keV),

does not necessarily reflect the ion bulk flow, in particular after the entry to hot plasma sheet. We therefore examine the ion distribution function and compare the ion moments with the ExB drift as well as with the current calculations from the magnetic field data in order to characterize the ion behavior in more detail later. Nonetheless, the overall direction of the ion bulk flow described above and the existence of the high-speed flows during this interval are still valid.

The 1-sec averaged electric field obtained from the electric field double probe instrument (EDP) [Ergun, et al., 2016; Lindqvist, et al., 2016] from MMS 3 is shown in Figure 2j. Intense electric fields, mainly in north-south direction with some enhancements in the duskward component, were observed during the FAC intervals. The enhancement of the northward electric field is associated with FAC event (i) and the southward turning of the electric field is associated with FAC event (ii). Event (iii) took place during the recovery of the southward electric field, but also during the largest enhancement in duskward electric field (-Ed). Event (iv) was observed associated with short-time scale enhancement in the electric field, first southward then northward.

Since the changes in the Bd component of the magnetic fields dominate among the other components in Figure 2e-g associated with the FAC events (i-iv), a planar field-aligned current sheets is a valid assumption, which expected to be in the near-Earth PSBL and the FAC is flowing approximately along V direction. In order to estimate the overall motion of the PSBL we applied the timing methods (See Schwartz, 1996 and reference therein). With the timing method orientation and motion of a planar boundary can be obtained using observation from the four spacecraft with some time-differences. That is, observations from spacecraft pairs α and β with a separation vector, $\mathbf{r}\alpha\beta$, are used to determine the time difference $t\alpha\beta$, where $\alpha = 1$ and $\beta=2, 3, 4$. The speed of the magnetic structure, which we call "timing velocity", $\mathbf{V}_{tim} = V_{tim}\cdot\mathbf{n}$, can then be determined by obtaining the solution of:

$$\begin{pmatrix} \boldsymbol{r}_{12} \\ \boldsymbol{r}_{13} \\ \boldsymbol{r}_{14} \end{pmatrix} \cdot \begin{pmatrix} n_x \\ n_y \\ n_z \end{pmatrix} = V_{tim} \begin{pmatrix} t_{12} \\ t_{13} \\ t_{14} \end{pmatrix} \qquad (1)$$

In order to examine the overall motion of the PSBL, we estimated the timing velocity every 2 s and the results are shown in Figure 2k. Here time differences between pairs of spacecraft are determined by cross-correlation of the Bd over time interval of 10s. Since, VDH is a local coordinate system, which differs for each spacecraft, we determine first the timing velocity in SM coordinate system and then transformed into the VDH coordinate system at MMS3. The normal component of PSBL or FAC layer is expected to be approximately the H component so that the motion of the FAC/PSBL will appear in the H component of V_{tim}. Although we have fixed the time-scales of the magnetic structure to 10s with this method, the overall motion of the PSBL is well reconstructed. That is, outward motion of the plasma sheet (negative Vth) during the event (i) and (ii) followed by inward motion during events

(iii) and (iv) and then later again outward motion of the plasma sheet when the Earthward flow subsides.

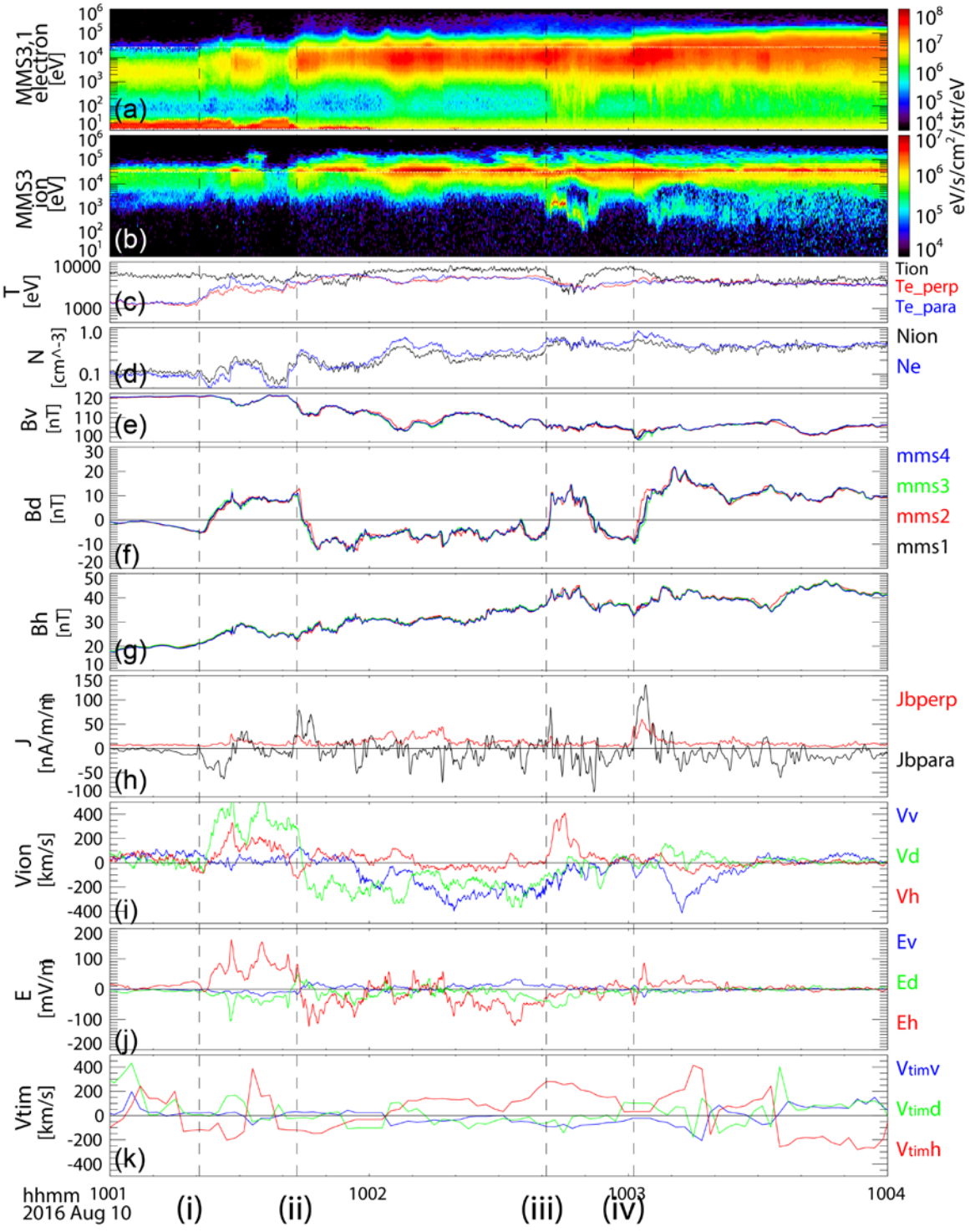

Figure 2. MMS observations between 10:01-10:04 on August 10, 2016. Energy spectra from (a) electrons and (b) ions obtained from EIS and FPI instruments. Electron spectra for energy lower/higher than 25 keV are plotted using FPI and EIS data. The EIS electron energy flux is multiplied by 2.75. Ion spectra for energy higher/lower than 30 keV are plotted using EIS/FPI data. (c) Electron perpendicular (red) and parallel (blue) temperatures, (d) ion (black) and electron (blue) density, (e) V, (f) D, and (g) H components of the magnetic fields from the four MMS spacecraft. (h) The parallel (black) and perpendicular (red) components of the currents determined using the curlometer method. V(blue), D (green), and H (red) components of the ion flow (i), the electric field (j), and the timing velocity (k). Plasma moments are calculated using FPI data. The vertical dashed lines show the start of the crossing times of the main current layers associated with the dipolarization: i) 10:01:22, (ii) 10:01:43 (iii) 10:02:41 (iv) 10:03:01.

In Figures 3a-c the V, D, and H components of E×B drift velocity (black curves) are compared with the plasma flow velocity perpendicular to the magnetic field obtained from FPI and HPCA [Young et al., 2014] measurements. While the HPCA scans plasmas up to 40 keV for different ion species, the energy channel of FPI ions and electrons are up to 30 keV. The E×B drift velocity and the electron (green curves) and ion (red curves) velocities data are boxcar-averaged over 0.6s. The time resolution of the proton velocity (blue curve) from HPCA is 10 s. As expected from the northward and then southward electric field, the overall flow direction was changing from the dawnward to duskward direction during event (i) and event (ii) and then recovered after event (iii). The ion velocity from FPI with lower energy coverage is mostly lower than the HPCA velocity and is likely underestimated, in particular after entering the plasma sheet proper, as discussed before. Nonetheless, it can be seen that the overall changes in the flow direction are similar among the four velocity estimates. Taking into the different time scale of the changes in Bd, the timing velocity, V_{tim}, was estimated for each event (Nak17) and shown as the horizontal bar in panels (a-c). They are obtained using the change in the Bd among the four spacecraft during the interval plotted by the horizontal bar in panels a-c. For events (i)-(ii), the direction of V_{tim} is southward (outward), tailward, and duskward, and opposite for the event (iii-iv). Plasma is moving northward/equatorward with respect to the boundary as expected in the enhanced dawn-to-dusk convection electric field (-Ed) for events (i)-(iii), while the FAC event (iv) took place after the convection electric field enhancement (see Figure 2j). The timing method assumes a planar boundary with a stable structure moving with one constant speed and hence, it is an average speed over the entire current sheet neglecting some internal structures. The boundary motion can reflect however also a temporal evolution of the current sheet such as the case for expansion of the plasma sheet. The electric field/plasma should reflect the motion of the overall current sheet and the equatorward convection as well as the internal processes within the current sheet. Therefore, an apparent difference between V_{tim} and plasma motion can take place during events (i), (ii) when plasma sheet expands outward while plasma is convecting equatorward.

The average ion velocity vector, V_{ion} (green), V_{tim} (red), and the magnetic field difference, ΔB (black), between the start time and end time of the FAC crossing interval, are shown projected on the V-H plane in panels d-g and on the D-H plane in panels h-k. The electric field, E (blue), is also shown in panels h-k. Note that these FACs (flowing mainly along V) are producing the magnetic disturbances predominantly along D, as can be seen in the black

arrow, ΔB, and hence the timing velocity along the H direction represents the motion of the current sheet. The spatial scale of the four current sheets was estimated using the H component of the V_{tim} and the duration of the B_D change (Nak17), which is highlighted as orange region in the bottom panels. The thicknesses of these currents sheets are (i) 1310 km, (ii) 710 km, (iii) 140 and (iv) 170 km. The black vertical bars correspond to the ion-inertial scale, while the red vertical bar shows the ion-gyro radius. It can be seen that the spatial scale of the FAC events (i) and (ii) are well above the ion scales, whereas the events (iii) and (iv) are comparable to or less than the ion-inertial scale and a couple of ion-gyro scales. Note that the relative thickness to the ion gyro radius may be smaller for events (iii) and (iv) due to possible underestimation of ion thermal velocity during these times. Hence at least for events (i) and (ii) the overall pattern of the intense dawnward flow and reversal to duskward flows and associated FACs are expected to be a large-scale process, although some ion-scale substructures are embedded in these events (see Le Contel et al. [2017] for detail). Based on these flow and field patterns at MMS, observations from ground and other spacecraft, and comparisons with an MHD simulation, NAK17 suggested that events (i) and (ii) detected at MMS are most likely due to the crossing of the high-latitude side of the current wedge produced in the flow-braking region.

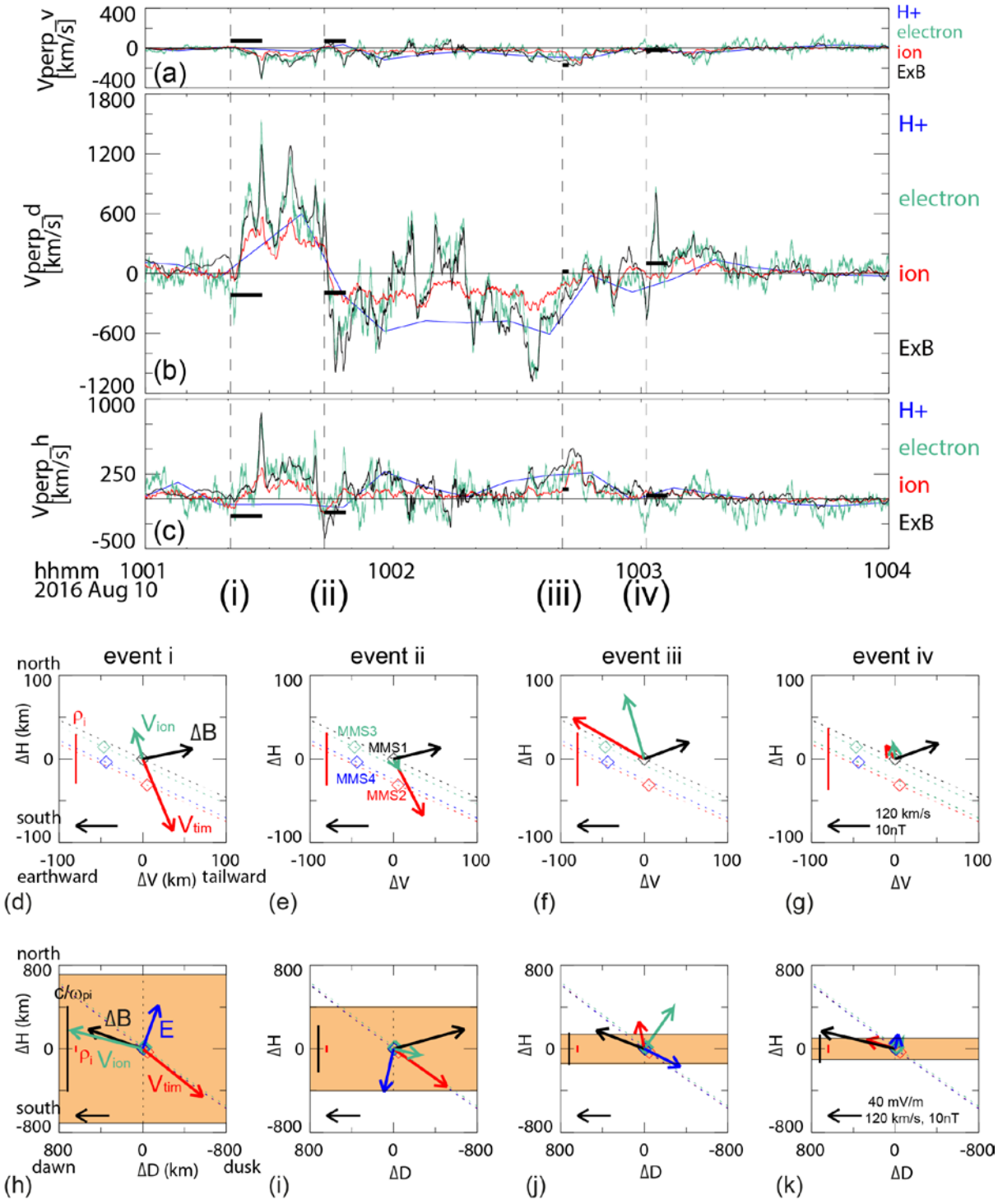

Figure 3. Motion of the plasma and the boundary structures during the four FAC events. (a) V, (b) D, and (c) H components of the flows perpendicular to the magnetic field. Black curves correspond to E×B drift, the red and green curves are the FPI ion and electron velocities, and the blue curves are the proton velocity from HPCA. The horizontal black bars in (a-c) represent the timing velocities and the vertical dashed lines indicate the start

times of event (i-iv). The average direction of the field and flow disturbances during the events (i-iv) are summarized in panels d-k. The average ion flows perpendicular to magnetic field (Vion, green), the timing velocity vector (Vtim, red), and the magnetic field disturbance vector (ΔB, black) during the four current sheet crossings (i-iv) are shown in panels d-g projected on the V-H plane and in panels h-k projected on the D-H plane. The electric field is also shown in dark blue in panels (h-k). The spatial scales: on ion-gyro radius (red) and one inertial length (black), are shown as vertical bars. The estimated thickness of the FAC sheet is presented as orange area. The relative locations of the spacecraft to MMS1 are also given together with the orbit direction (dashed line) in panels d-g.

In addition to the overall dawn-dusk reversals that are seen in the ion, electron, and E×B-drift velocities, there are shorter time-scale disturbances detected in the E×B (and electron) flows when there is a significant deviation between them and the ion (and proton) velocity. In these plots, all velocities are averaged over one second, which is still larger than the average ion gyroperiod of ~0.6 sec. The electron perpendicular velocity changes follows most of the time with the E×B drift changes. There are also sharp peaks when the electron and E×B drifts deviate, suggesting the existence of smaller scale processes. Around event (iv), the dawn-dusk flow reversals show very good coincidence between the electron and the E×B drift under the condition of nearly zero ion velocity, indicating that the profile is due to Hall effects as will be discussed more detail in section 4.

3 FAC layers and characteristics of electrons

In order to examine the characteristics of the FAC layers, we examine the plasma population responsible for carrying the current and compare with the curlometer currents. Figure 4 shows the parallel currents and electron pitch-angle distribution. The parallel current (panel a), J_para, obtained by curlometer (labeled as curlB, blue curve) agrees well with the total plasma (mms3_p, green) current, which is predominantly carried by electrons (mms3_pe, red). Hence, for the parallel current the effect of possible underestimation of the ion current (mm3_pi, black) due to the limited energy range is negligible as the parallel electron velocity is much larger than the parallel ion velocity. The electric current data shown in Figure 4a are averaged over 0.5s to be comparable to the ion-gyro period. The particle currents are calculated from MMS 3 data. The curlometer current, on the other hand, approximates the current at the barycenter and is obtained assuming linear gradients in B over the spatial scale of MMS, i.e., about 50 km. The overall agreement between the particle and curlometer current density profiles for the four FAC current sheets therefore suggests that the four current sheets have spatial scale sizes of ions or larger, as expected from the estimation of the current sheet scales shown in Figures h-k. Yet, electron currents show additional short-time scale fluctuations such as those seen in the later part of event (iv). In fact, the electron currents parallel to the magnetic field, Je_para, are highly structured during most of the interval except for event (i) as shown in Figure 4b, wherein the electron parallel currents are depicted using 0.1 sec averaged data from FPI for different energy range: higher energy (2 - 30keV) shown in green, lower energy (200eV- 2keV). Figure 4 c-g shows changes of the energy and pitch angle distribution of electrons for the selected energy ranges. Pitch-angle spectra are shown for energy range of (d) 119 keV - 129 keV and (e) 65 keV – 75 keV, obtained from the EPD/FEEPS instrument [Blake et al., 2016] aboard MMS2 depicting the non-thermal electron pitch-angle signatures and for (e) 2keV-30keV and (f) 200eV-2keV

obtained from FPI measurement aboard MMS3 depicting the thermal part of the electron signatures.

The electrons responsible for upward and downward currents are quite different in their energy ranges, as can be seen in Figure 4b. In general, the higher-energy population (2keV-30keV) contributes mainly to the upward (parallel to field line) current, while the lower energy (200-2keV) electrons are the dominant carrier of the downward current during most of the times, though the populations associated with the short-time scale fluctuations in the FAC are more variable. Since the Earthward fast flows indicate that MMS was Earthward of the near-Earth reconnection region, the higher-energy electron populations streaming Earthward (contributing to upward FAC) may correspond to electrons accelerated in the reconnection region [e.g. Hoshino et al., 2001] and due to Fermi type acceleration for non-thermal trapped population associated with the reconnection jet [e.g. Fu et al. 2011]. Possible sources of the cold electrons streaming tailward (downward FAC) are ionospheric population accelerated by the kinetic Alfven waves observed at PSBL[e.g., Wygant et al. 2002] and the lobe population accelerated along the field line due to the large-scale electric field [Egedal et al., 2012] or localized double layer [Fujimoto, 2014] at the Earthward side of the reconnection region.

The four FAC events (i-iv) are associated with distinct changes in the energies of electrons as well as the pitch-angle distribution, resulting in stepwise enhancements in energy. FAC event (i) is associated with enhancements in the low-energy parallel electrons (panel g), producing the downward current. Event (i) is followed by upward FACs associated with enhancements in the higher-energy electron (above few keV) population in the parallel/anti-parallel direction (panel f). It is interesting to note that around 01:28 UT there is a distinct downward current peak associated with parallel (tailward) moving energetic electrons up to 75 keV, as can be seen in Fig.4e. This electron signature requires therefore a tailward acceleration, opposite to the general trend mentioned above. More detail on this event is provided by Le Contel et al. [2017]. FAC event (ii) is associated with enhancements in the anti-parallel electrons of a few 10s keV (panel f), followed by enhancements in the parallel and anti-parallel portions of the electron population in the 65 keV – 75 keV range (panel e). The later two events, however, are associated with enhancements in suprathermal electrons centered at a 90^{o} pitch angle, as can be seen in panel e for event (iii) and panel d for event (iv). The magnetic field magnitude during event (iv) increases with the dipolarization, indicating that this is likely a betatron effect.

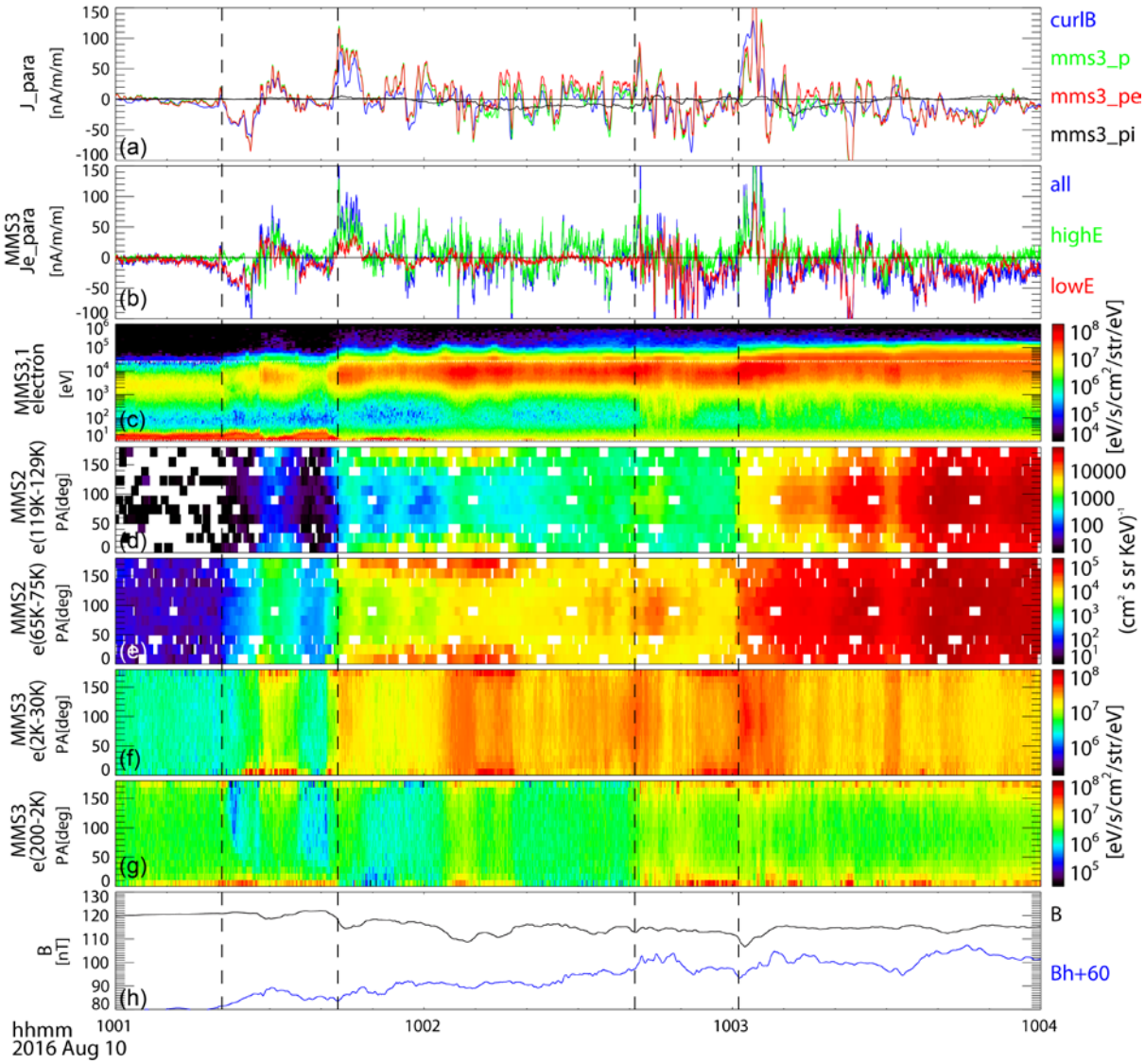

Figure 4. Parallel currents and spectral characteristics of electrons. (a) Parallel current density estimated using FGM data from the four MMS applying the curlometer method (blue), and currents calculated from ions (black) and electrons (red), and total of ions and electrons (green) from FPI measurements of MMS 3. (b) Electron parallel currents from FPI for different energy range: higher energy (2 - 30keV) shown in green, lower energy (200eV- 2keV) shown in red, and all energies shown in blue. (c) Electron energy spectra using same format as in Figure 2a. Electron pitch-angle spectra for the energy range of (d) 119 keV - 129 keV and (e) 65 keV – 75 keV obtained by the MMS 2 EPD/FEEPS instrument and for (f) 2keV-30keV and (g) 200eV-2keV obtained by MMS 3 FPI measurement. (h) Magnitude (black) and BH (blue) component (added by 60 nT) of magnetic field from MMS. The vertical lines indicate the four FAC events.

4. Characteristics of perpendicular currents

Figures 5a-5c show the perpendicular current density estimated from the curlometer method and the particle measurements in the GSM coordinate system. As expected in the nominal

magnetotail current sheet, the perpendicular component of the curlometer current, Jb_perp (panel a), shows that the current is predominantly in the dawn-to-dusk direction (green component), except for during short peaks such as the beginning of event (iv). The magnitude and Y_{GSM} component of the perpendicular currents, J_perp and Jperp_y, deduced from particles and from the curlometer method are compared in panel b and panel c, respectively. Total particle current (mms3_p, green) and curlometer current (curlB, blue) show mostly comparable values (Fig. 5b). Yet, the dawn-dusk current shows some inconsistency in the direction during the interval when dawnward Jperp_y current was observed for particle current, while the curlometer current shows predominatly duskward current between events (ii) and (iii). These difference may likely come from the underestimation of the ion current (mms3_pi, black trace) which can be seen from the difference in the ion velocity obtained from FPI and that from HPCA during this interval as shown in Figure 3b. It can be seen that most of the transient enhancements in the dawn-dusk component of the curlometer currents are associated with enhancements in the electron currents suggesting that these are the Hall current layers.

To examine the signatures of the Hall-current in a more quantitative way, we examined the contribution of the Hall-term in the generalized Ohm's law and shown in panel d. Here we examined the Z component, which is the main component of the electric field during this observation. Here we compare $E + Vi \times B$ (blue curve) with the Hall-term calculated from the particle current, $Jp \times B/eN$ (green), and from the curlometer current, $Jb \times B/eN$ (red). Those times when $E + Vi \times B$ agrees both with $Jb \times B/eN$ and $Jp \times B/eN$ within 30% are marked with the tick marks at the bottom of panel d. Many of the transient dawn-dusk current enhancements shown in Figures 5a-5c are associated with the times when the Hall-term dominates in the generalized Ohm's law, i.e., $E + Vi \times B = J \times B/eN = (Vi - Ve) \times B \neq 0$. In order to compare the Hall-electric field with the convection electric field, we plotted also $-(Vi \times B)$ as black trace in panel d. The maximum Hall-electric field, $J \times B/eN$, from the curlomenter current was 133 mV/m, which was about the double of the maximum convection electric field ($-Vi \times B$), 66 mV/m, for the data shown in Figure 5d. The importance of the Hall-effect, however, differs among the events. For example, the Hall-electric field is about double the amplitude of the convection electric field $-(Vi \times B)$ for those times indicated by the tickmarks between event (i) and (ii), but the Hall-electric field completely dominates during the later events, in particular those around 10:03 UT.

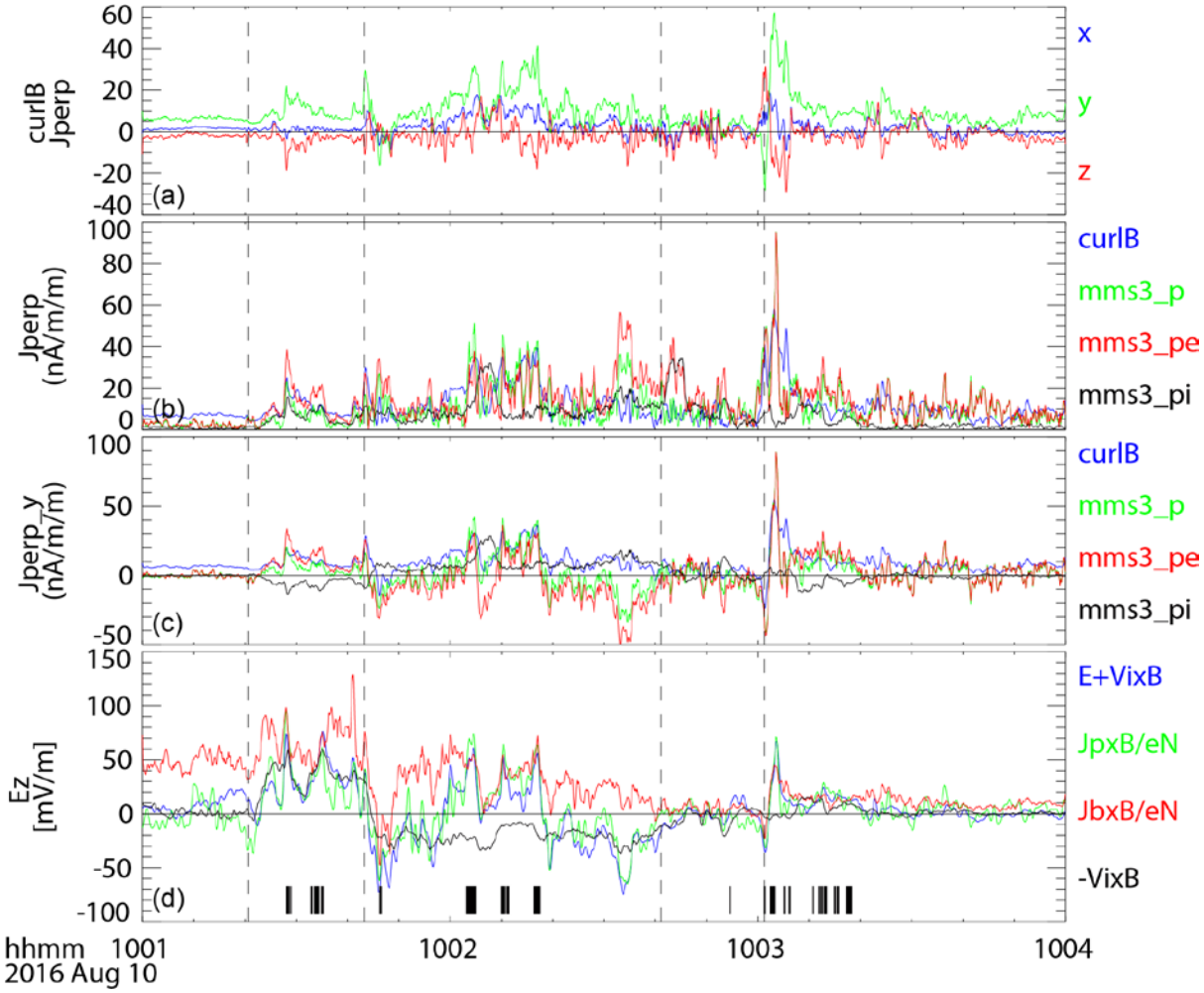

Figure 5. Perpendicular current density estimated using FGM data from the four MMS (curlometer method) and using FPI measurement from MMS3. (a) X_{GSM} (blue), Y_{GSM} (green), Z_{GSM} (red) components of the perpendicular current density obtained from the curlometer method, (b) magnitude of the perpendicular current density, (c) Y_{GSM} component of the perpendicular current density estimated from the curlometer (curlB, blue), ion and electron data (mms3_p, green), electron (mms3_pe, red), and ion (mms3_pi, black). (d) Z_{GSM} components of the perpendicular electric field: E + Vi × B (blue), where E is the measured EDP electric field, Jp × B/eN (green), Jb × B/eN (red), and -Vi × B electric field (black). The black bars in (d) indicates times when the E + Vi × B coincides with both Jb × B/eN and Jp × B/eN within 30%. The vertical lines indicate the four FAC events.

The Hall current features are further examined using 2D cuts of the velocity distribution during selected times around FAC events (i) and event (ii) in Figure 6. The energy spectra, the V, D, and H components of the perpendicular velocity and parallel currents, Jpara, are also shown in Fig 6. We present the ion distribution functions averaged over 4 data points, i.e., 0.6 sec (approx. 1 ion gyroperiod), to enhance the count rate of the ions but still frequent enough to the resolve the ion-scale feature. The velocity distribution functions (VDF) are

shown in the local field-aligned coordinate system. Here we defined the Vperp1 by the E × B direction, Vperp2 by the B × (E × B) direction, and Vpara by B. The cut of the distribution function is the average of phase-space densities within ±20 degrees relative to the plotted plane. For the E and B directions, 0.6-sec averaged electric field and magnetic field data are used. Note that the E × B direction coincides most of the time with the perpendicular velocity of the electrons (see Figure 3). Hence, the obtained VDF profiles in ion enable to examine the existence of Hall-currents, to confirm the magnetized/unmagnetized signatures of the ions, to check whether the ions consist of single component or multi-components, as well as to check the effect of the background.

During the FAC event (i) the E × B drift and ion and electron perpendicular velocities were enhanced as shown in panels (c-e). As expected, the ion VDF at t_A (panel g) has a peak in the direction of Vperp1 close to the E × B drift speed (vertical dashed line in the Vperp1-Vperp2 panel, and horizontal dashed line in the Vpara-Vperp1 panel). The deviation between the E x B drift and ion velocity becomes larger around t_B (panels c-e), which can also be seen in the 2D cuts of VDF at t_B (panel g). That is, there is a peak in VDF at t_B, which is smaller than the ExB drift as can be seen in the location marked with a red "X" in the Vperp1-Vperp2 and Vpar-Vperp1 panels from t_B, showing the peak along Vperp1 axis. The VDF peak at lower values than the E × B drift can be also seen in the VDF cut at t_C in the Vpar-Vperp1 plane. The time t_C corresponds to FAC event (ii), just before the reversal of the dawn-dusk flows. These deviations of the ion perpendicular velocity from the E×B drift, which was comparable to the electron perpendicular velocity, are expected for the Hall-current layer. The peak in VDF at t_D, on the other hand, coincides with E×B drift peak. That is, during this time the difference between the ion and electron drifts, and thus the Hall-current should have been decreased, which is consistent with the low level of the curlometer current shown in Figure 5. Note that the effect from the background (red areas at the center, i.e. low energy portion) becomes visible near t_C and is further enhanced for t_D, suggesting that the ion velocity may be underestimated causing the large deviation of the particle current from the curlometer current shown in Figure 5. In spite of these limitations, these observations clearly show that there are ion-scale Hall-current layers embedded in the reversal region of the FAC layers between event (i) and event (ii) where ions move slower than E×B drift, i.e., the electron motion.

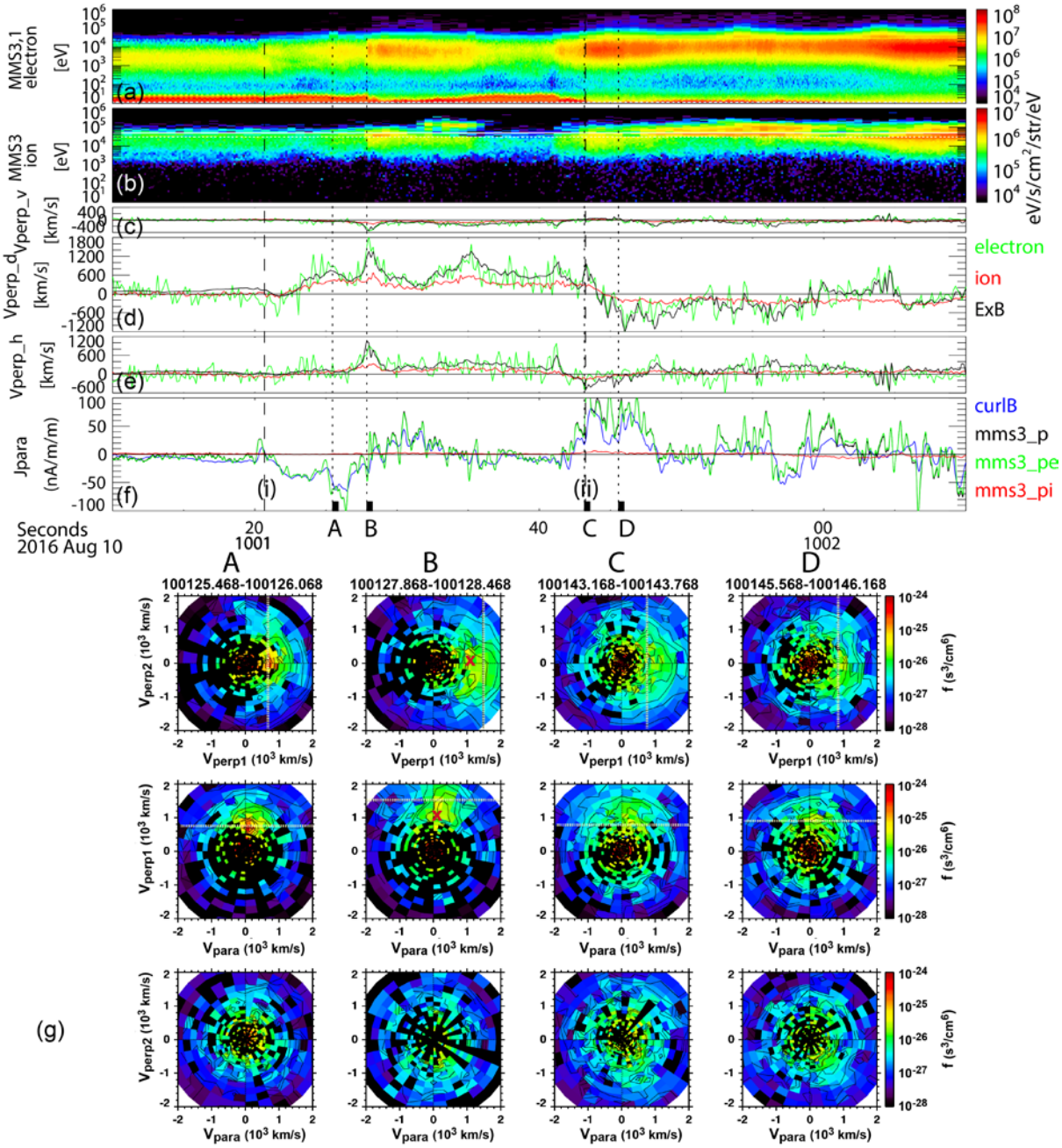

Figure 6. (a) Ion and (b) electron energy spectra, (c) V, (d) D, (e) H components of the perpendicular velocities of particle and E x B drift, and (f) parallel current densities estimated by curlometer and plasma. (g) Ion distribution during the selected times: t_A, t_B, t_C, t_D marked at the bottom of panel f, presented for three cuts in the Vperp1–Vperp2 plane, in the Vpara–Vperp1 and in the Vpara–Vperp2 from top to bottom. ExB velocity is marked as a dashed line. "X" in the VDF cut t_B in (g) shows the location of the peak around Vperp1 discussed in the text.

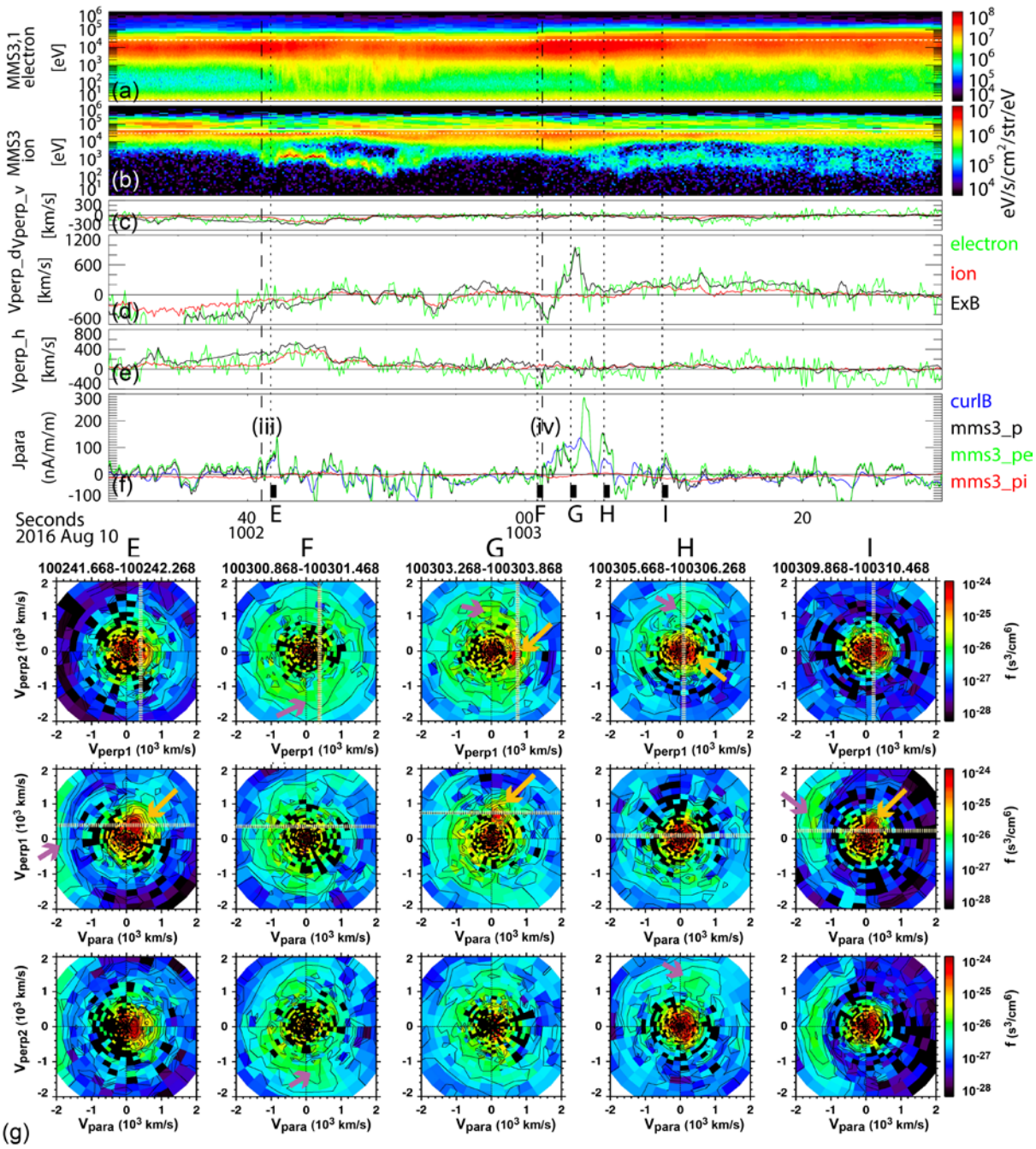

Figure 7. (a) Ion and (b) electron energy spectra, (c) V, (d) D, (e) H components of the perpendicular velocities of particle and E x B drift, and (f) parallel current densities estimated by curlometer and plasma. (g) Ion distribution during the selected times: t_A, t_B, t_C, t_D marked at the bottom of panel f, presented for three cuts in the Vperp1–Vperp2 plane, in the Vpara–Vperp1 and in the the Vpara–Vperp2 from top to bottom for ions spectra (g) and Vpara-Verp1 for electron spectra. ExB velocity is marked as dashed line. Cold ion and hot ion components discussed in the text are indicated by yellow and pink arrows in (g).

Particle velocity distributions around the FAC events (iii) and (iv) are presented together with the energy spectra, perpendicular velocity, and parallel current in Figure 7 in the same format as Figure 6. The most significant difference in the ions for the FAC events (iii) and (iv) compared to the previous intervals shown in Figure 6 is the existence of the cold component. They become prominent, as can be seen in VDF plots, at t_E and t_I (panel g, indicated by yellow arrows). For both events (iii) and (iv), hot ions tend to move anti-parallel (Earthward, indicated by pink arrows in panel g), while the cold ions are slowly moving parallel (tailward) suggesting that the hot ions are coming from the tail reconnection region and the cold ions from the direction of the ionosphere. The perpendicular velocity of the cold ions coincides well with the E×B drift as can be seen in Vpara-Vperp1 plots in panel g. As discussed before (Figure 3) the FAC current sheet of event (iv) is comparable to the ion-inertia as well as a couple of thermal ion gyro radii and corresponding non-magnetized ion signatures can be seen in VDF from t_E, t_F and t_G in the hot ion components. The VDF from t_E shows that the hot ion component is relatively isotropic, but instead of moving duskward ($-V_D$) with the E×B drift, the distribution shows motion in the -Vperp2, -Vpara direction, corresponding to equatorward and Earthward motion. The subsequent large E×B drift enhancement in the dawnward ($+V_D$) direction (panel d) coincides well with the motion of the cold-ion population seen in the Vperp1 direction in the VDF plots at t_F. Again, the hot population does not drift with ExB but is distributed along the Vperp2 direction as expected in a thin current sheet of non-magnetized ions, which can be seen most clearly in the VDF plots at t_G. Hence, a slower perpendicular speed of the net ion population relative to that of the magnetized electron is expected. The net perpendicular current is therefore mainly the sum of the E×B-drifting cold ions and electrons. It should be noted, however, that except for at t_F, the background effect is again still visible, hence the ion velocity is likely underestimated, resulting in some visible differences between the curlometer current and the particle current in Figure 5.

5 Discussion

MMS encountered multiple intense FAC layers in the outer plasma sheet of the near-Earth flow braking region during an intense substorms (AE > 1000 nT) on August 10, 2016. From multipoint data analysis of MMS, GOES 14,15 and Geotail in the nightside magnetosphere, and ground-based observations, (Nak 17) studied the evolution of the substorm current wedge. Associated with expansion of the plasma sheet, MMS first encountered downward and upward field aligned currents (events i and ii). It was shown that the overall changes of the disturbances of flows and magnetic fields, and north-south electric field, observed during events (i and ii) are similar to those predicted from the MHD simulation by Birn and Hesse [2014] of the near-Earth flow braking of the localized reconnection flows (Nak 17). It is also suggested that the successively reconnected field lines can result in outward motion of the boundary (plasma sheet expansion) in the flux pile up region in spite of enhanced inward plasma motion in the off-equatorial outer plasma sheet such as shown in MHD simulation [Birn et al., 2013].

While the MHD model proved the context of the overall observations (NAK17), transient disturbances and intense smaller-scale current sheet signatures are prominent in the MMS observations. For example, several thin duskward/dawnward Hall-currents were identified as shown in Figure 5. In order to discuss possible signatures to be observed around the outflows of reconnection (reconnection jets), when the Hall effect is considered, we refer to the simulation results in Figure 8 showing a localized jet in an MHD simulation by Birn and Hesse [2014] and in a Hall MHD simulation by Nakamura et al. [2012]. The top three panels of Figure 8 show (a) By disturbances in the X-Z plane at the dusk part of a reconnection jet and (b) By and (c) Ez disturbances in the Y-Z plane from the large-scale MHD simulation by Birn and Hesse [2014], where the detailed setting is described. In this simulation, the near-Earth reconnection region is formed at X~-20 and a localized flow burst near midnight reaches the near-Earth region X=-10 by t=130. Panels b and c are taken from this time and location to show the effect of the dipolarization front and flow vortices surrounding the flow burst in the near-Earth region, where MMS is expected to have been traversing (indicated by an arrow in panel b). As discussed in (Nak17) these patterns well represent the overall observation associated with the expansion of the plasma sheet. That is, the direction of the dawn and then duskward perturbation in By component (Figure 8b) accompanied by changes in northward and then southward electric field (Figure 8c) are consistent with the observations as summarized in Figures 3d, h, and i, by taking into account the northward motion of the spacecraft relative to the current sheets (as presented in the arrow in Figures 8b-c).

Similar figures of the fields and flow patterns, but from a Hall MHD simulation by Nakamura et al. [2012], are shown in Figures 8d - 8i from the Run 2 in their paper. In this run the reconnection starts from a current sheet with a half-thickness of 1di (ion inertial length) and from a 8 di wide region, located at X=80 di and Y=75 di. The reconnection region then expands dawnward (-Y) along the same direction as the current-carrying electron motion. The snapshots shown in Figure 8 are after 55 ion gyro time, at which point a localized reconnection jet has developed well without being affected by the simulation boundaries. The jet properties shown here are downstream of the reconnection region by about 30 di, i.e., ~3 R_E (for density value of 0.1/cc corresponding to beginning of this event). The simulation starts with a 1D current sheet configuration (without initial By and Bz components), which is in contrast to the large-scale modeling of tail field and superposed dipole field setting by Birn et al. [2011]. Nonetheless, the perturbation around the head of the reconnection jets still demonstrates the effects of the Hall-field on the interactions between the localized reconnection jets and the ambient plasma as will be discussed below.

Figures 8d-8f show the B_Y perturbation in the X-Z plane at the dusk part of the ion jet and the B_Y, and Ez disturbances in the Y-Z plane, similar to the MHD simulation. The possible MMS crossing direction, which is in the southern hemisphere dusk portion of the flow in the Y-Z plane is indicated by a black arrow in Figures 8e-f and 8h-i. Due to the duskward tilt of the localized ion jet from the dawnward-expanding reconnection region, a significant dawn-dusk asymmetry is visible. Still we can identify a similar convection effect by the localized reconnection jet as in the MHD case, in addition to the Hall effects, as will be described

below. B_Y perturbations in the X-Z planes (Figure 8d), taken from the dusk part of the flows, show an extension of the quadrupole field visible from the ion diffusion region at the poleward side (blue/red region in southern/northern hemisphere) and inverse Hall field due to jet braking in the equatorward side (red/blue region in southern/northern hemisphere). Here we call this pattern a 2D Hall effect of the reconnection jet. The B_Y perturbation created by the Hall effect, however, has the same perturbation signatures as that created from the localized flow in the +Y region (duskside) as can be seen in Figure 8b and 8e along the black arrow. B_Y perturbation in the Hall-MHD simulation (Figure 8e) shows that the 2D Hall effect is embedded in the localized flow effect, which results in also an asymmetric Ez pattern in the dawn-dusk direction (Figure 8f). To separate these two effects: i.e., contribution to Ez by the Hall and localized flow effects, Figures 8h and 8i present Eh_Z =-(Ve-Vi) x B (Hall field) and –Vi x B (convection electric field), respectively. It can be seen that Figure 8i more closely resembles the MHD case (Figure 8c), while Figure 8h shows the quasi-2D Hall electric field pattern as expected. When crossing the dusk and southern part of the boundary as indicated by the black arrows in the Y-Z planes in Figure 8, the convection part of Ez (Figure 8i) has positive to negative variations, which is similar to the MHD case (Figure 8c). The Hall electric field part (Figure 8h) features only a strong positive value with the peak located near but equatorward of the positive peak of the convection Ez. Hence the Hall-electric field part looks to be embedded in the localized flow part in Figure 8f.

The observed characteristics of the FAC events (i) and (ii) and the embedded Hall-current layers are summarized in the drawings in Figure 9a. While the observations do not conform to such a simple pattern as the simulation, the stronger equatorward electric field ($+E_H$) compared to the outward electric field ($-E_H$) shown in Figure 2j is consistent with the prediction from the Hall MHD simulation on the duskside of the reconnection jet, even though the structures feature larger dawn-dusk asymmetries than the MHD simulation. Also, the small-scale embedded Hall-current sheets observed between the events (i) and event (ii), as discussed in Figure 3, 5, and 6 indicate that the region of the equatorward electric field (where Hall effect to be expected) consists of ion-scale boundaries similar to that in the Hall-MHD simulation. The Hall effect is dominant in the localized reconnection simulation by Nakamura et al. [2012]. The observations also obtained larger Hall-electric field than the convection electric field, whereas the relative importance was quite variable depending on the types of the current sheet as discussed in Figure 5.

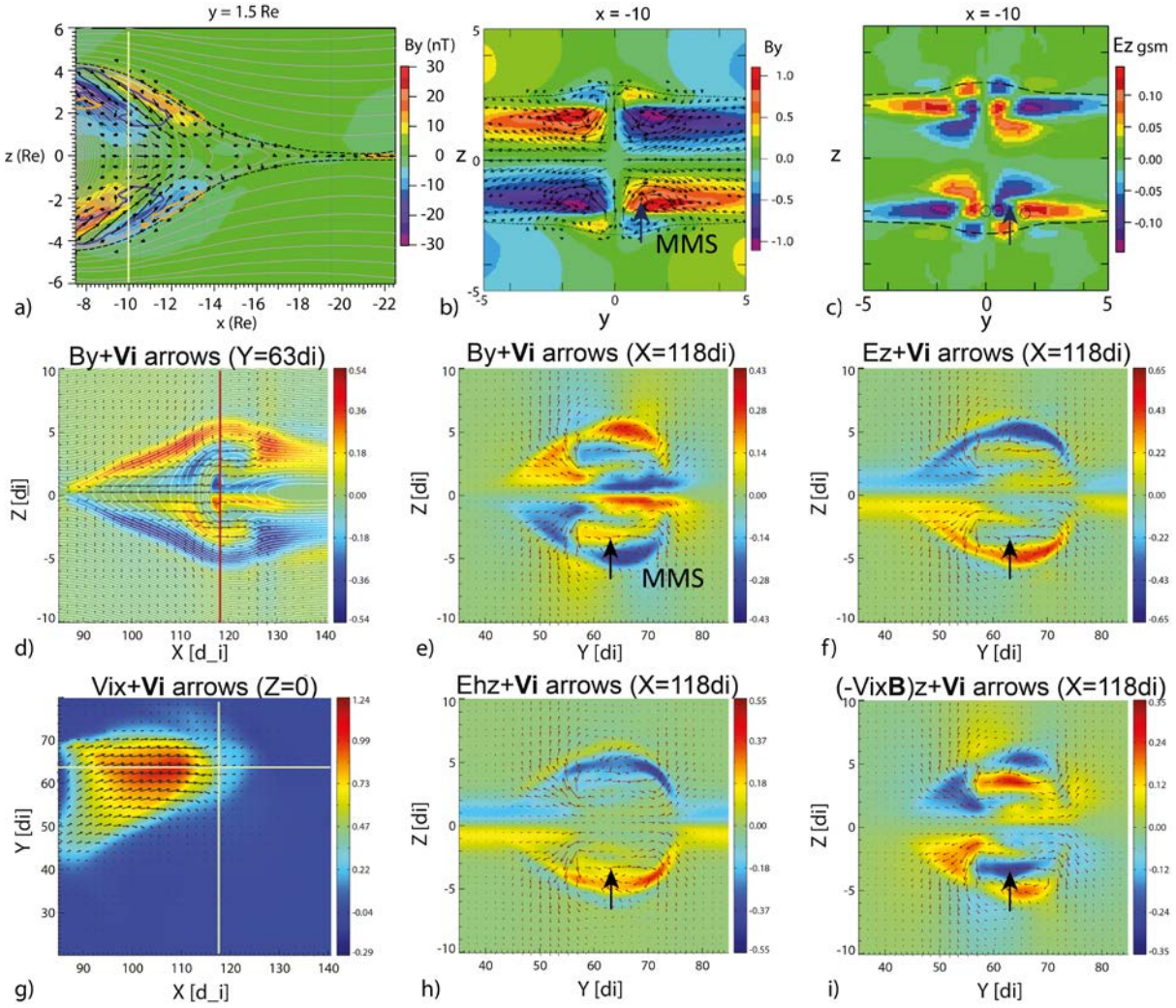

Figure 8. Reconnection jets in magnetotail MHD simulation by Birn and Hesse [2014] and in Hall MHD simulation by Nakamura et al. [2012]. (a) Color-coded By in X-Z plane at t=132 at y=1.5 together with the current density vectors (Δj) akin to Figue 8a of Birn and Hesse [2014]. Dark blue and orange contours indicate regions of enhanced tailward and Earthward FACs, respectively. Color-coded (b) By (normalized to 20 nT) and (c) vertical (northward) electric field Ez (normalized to 20 mV/m) in the Y-Z plane at t=132 at X=-10 from the same MHD simulation. (d) Color-coded By in X-Z plane at Y=63 di, (e) By and (f) Ez in the Y-Z plane at X=118 di, (g) Vi in the equatorial plance, (h) Ehz and (i) (-Vi×B)z in the Y-Z plane at X=118 di from Hall MHD simulation by Nakamura et al [2012]. Possible MMS location and direction of the crossing during events (i-ii) in the Y-Z plane are shown as black thick arrows in (b, c, e, f, h, and i). The thin arrows in (c, d) show the E×B drift vectors, while the other vectors are Vi flows. The color-scale of By shown in (d, e) is normalized to the initial magnetic field outside the current sheet, B_0, and the Vix in (g) is normalized to the Alfven velocity outside the current sheet, $V_A \sim B_0/(N_0)^{½}$, where N_0 is the density outside the current sheet, and Ez in (f, h, and i) is normalized to $V_A B_0$.

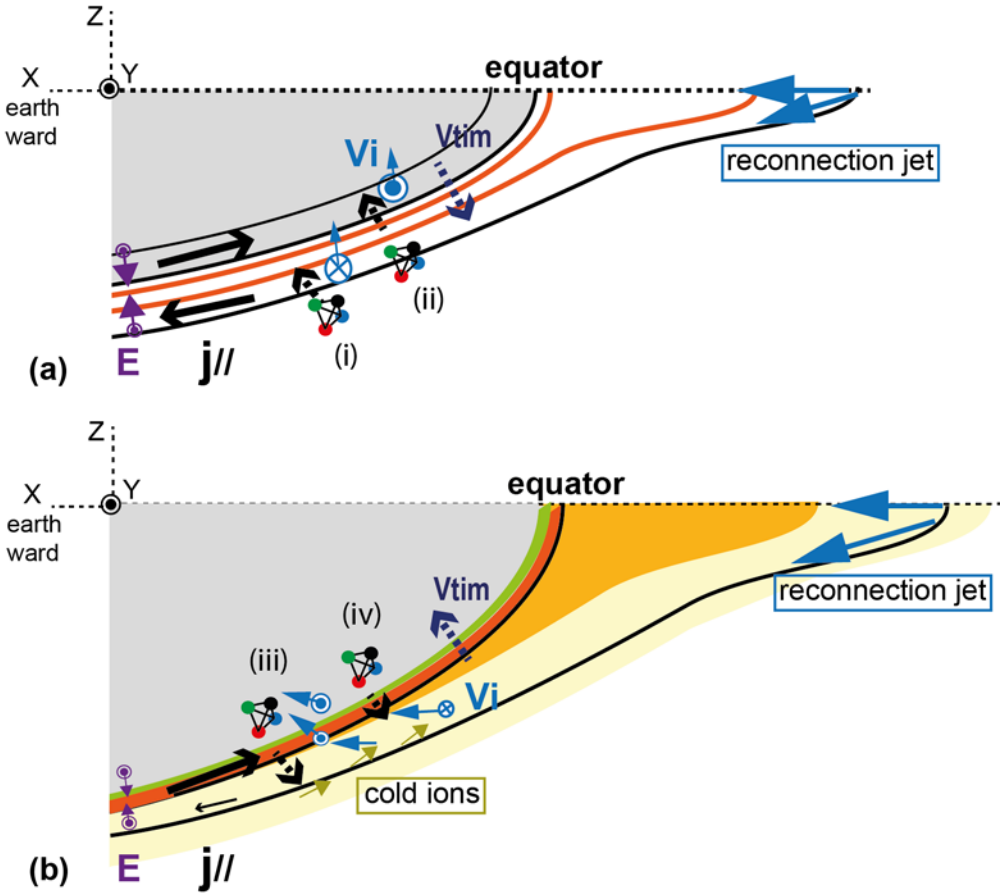

Figure 9. Schematics showing the main observational characteristics of (a) the FAC events (i-ii) and (b) the FAC events (iii-iv) and the ion-scale thin (Hall) current layers flowing duskward (red) and dawnward (light green). FAC directions are given by the black arrows. The dotted arrow shows the spacecraft motion relative to the current sheet, i.e. the motion of the current sheet itself is outward for the events (i-ii), and inward for events (iii-iv). The ion bulk flow is given in blue arrows, while the purple represents the electric field direction. Light yellow are in (b) represent region with tailward cold ion beams.

The scale size of the current layers of events (iii) and (iv) are, on the other hand, comparable to or below the ion inertial length and larger than the ion-gyro scale. As expected for this spatial scale size, the VDF (Figure 7) showed features of unmagnetized ions, moving along the electric field direction. Figure 9b illustrates the observational characteristics of the FAC events (iii) and (iv). Further differences from the events (i) and (ii) are that the current sheet motion was inward, i.e., in the same direction as the convection. The crossing of the FAC layers (iii) and (iv) are followed by the appearance of the hot Earthward-moving ion beams, together with the cold ions and electrons as also shown in Figure 7. These cold ions are streaming tailward and drifting with ExB drift. Such cold ions have been identified in PSBL; they are streaming from the ionosphere and become visible when the electric field is sufficient to gain E×B energy above the detector energy range [Sauvaud et al., 2004]. One should, however, note that the cold ions are only visible following the FAC events (iii) and (iv), but not during events (i) and (ii), when the E×B drift should have been even larger. Hence, for the case we studied, the cold ions seemed to exist only on the flux tubes MMS

encountered during events (iii) and (iv). We suggest that the events (iii) and (iv) are the inner boundary of the equatorward/inward convecting flux tubes resulting from reconnection involving lobe or PSBL field lines with enhanced ionosphere outflows related to global wind [Moore and Horwitz, 2007] or due to direct ion injection [Sauvaud et al., 2004]. In the direct injection case, however, the time scale of such ion upward accelerations is larger than 10 min to be observable at MMS. That is, the sudden encounter of the cold ions is not due to the sudden injection itself but rather due to encounter of the flux tubes already filled with the cold ions as illustrated in Figure 9b. This scenario, where multi component ions generate a Hall current in the exhaust far downstream of the reconnection x-line, has been studied in numerical simulations [Fujimoto and Takamoto, 2016; Higashimori and Hoshino, 2012]. In such Hall-current exhaust, the ion drift velocity is modified around the current layer due to a finite Larmor radius effect [Fujimoto and Takamoto, 2016]. Our observation also showed such Hall-current layer with the mixture of unmagnetized hot ions and magnetized cold ions E×B drifting together with electrons as given in Figure (7g, t_G) during event (iv) as sketched as red region in Figure 9b. It is interesting to note that the most unmagnetized distribution of ions was found at the beginning of event (iv) as shown in Figure (7g, t_F) and illustrated in Figure 9b as a green flux tube. It corresponds to the strongest dusk-to-dawn currents (Figure 5). During this time, the ions tend to move along –Vperp2, i.e. Earthward/equatorward, as if keeping the original motion of the reconnection jet rather than drifting with E×B. These features are consistent with the mechanism responsible for creating the opposite Hall-field at the head of the reconnection jets where unmagnetized ions overtakes the magnetized electrons, which has been shown in numerical simulations [e,g., Nakamura et al., 1998]. The resultant magnetic field disturbance, opposite to those in the ion diffusion region near the X-line, can be also seen at the equatorward side of the leading part of the jet in Figure 8d (as discussed before). The best agreement with electron perpendicular motion and E×B drift was achieved for the thin perpendicular currents during event (iv) among all the thin currents (Figure 7d). During event (iv) therefore only the magnetized electron drift contributes to the Hall-current.

While we have so far concentrated on processes with ion scales or larger, the above description may need some modification once shorter time variations are taken into account. For example, the first type of Hall-current described above contains highly structured electron currents due to interactions with lower-hybrid waves, which was obtained based on the high-resolutions particle and field data [Le Contel et al., 2017]. In the presence of high-frequency wave activity, our averaged data processed beyond ion-gyro time scales may smear out the responsible electric fields and may cause differences between the ExB drift and the electron motion in addition to the possible contribution from electron-scale processes. Such wave activity was, however, weaker for event (ii) [Le Contel et al., 2017]. The overall agreement between the electric-field drift and electron perpendicular velocity shown in Figure 3, and the agreement between the curlometer current and the particle current during the intense dawn-dusk current events indicated in Figure 5 suggested that the overall processes of these intense current events can be well described with Hall-physics once different ion components are taken into account.

The four FACs have also differences in the non-thermal signatures of electrons. All the fronts are associated with the enhancements in the electron energy: events (i) and (ii) are associated with enhancements in parallel/antiparallel component, while events (iii) and (iv) are associated with appearance of an enhanced perpendicular population. Previous observations of dipolarization fronts in the inner plasma sheet also showed energetic electron enhancements of different pitch angle population [Fu et al., 2011; Runov et al., 2013]. The two types of populations have been interpreted to be due to different electron acceleration mechanisms: Fermi and betatron mechanisms. Fu et al. [2011] suggested that the pancake-type (maximum in 90º pitch angle) pitch-angle distributions (PADs) appear mainly inside the growing flux pile up region (FPR) where the flow velocity is increasing and the local flux tube is compressed. The cigar-type (maxima at 0º and 180º pitch angle) PADs occur mainly inside the decaying FPR, where the flow velocity is decreasing and the local flux tube is expanding (flow braking). Runov et al. [2013] reported that pancake-type and cigar type PADs coexist at the dipolarization front, and that the PADs are mainly pancake type near the neutral sheet (Bx < 5nT) and mainly cigar type outside (Bx >10 nT). Both observations are from dipolarization fronts relatively near to the center of the plasma sheet, which is different from our observations. Yet, there are certain similarities to our observations in the outer plasma sheet. As discussed before, events (i) and (ii), which contain cigar-type PADs, are likely associated with flow braking as suggested by Fu et al. [2011] and away from the neutral sheet [Runov et al., 2013]. While events (iii) and (iv), which observed pancake-type PADs, took place not in the neutral sheet, but the field is in a more dipolar configuration (larger Bz) and it is at the inner edge of exhaust, which are similar condition to the pancake PAD observations by Runov et al. [2011] and by Fu et al. [2011]. Hence, we may have detected equivalent acceleration processes to those observed in the dipolarization front at the center of the plasma sheet. It is interesting to note that these different types of the fronts were sequentially detected within a relatively short time in our observation.

6 Conclusions

MMS resolved the characteristics of intense current layers within the dusk part of the substorm current wedge of a substorm during fast flow disturbances (up to about 500 km/s), mostly in the dawn-dusk direction. MMS first encountered downward and upward field aligned currents associated with expansion of the plasma sheet followed by upward field aligned current layers on the thin equatorward convecting flux tubes, preceding PSBL-type Earthward streaming hot ions and tailward streaming cold ions. The field-aligned currents are initially associated with expansion of the plasma sheet and the flow and field disturbances showed distinct pattern expected in the braking region of localized flows. Supporting evidence was found in the simulated signatures of reconnection jets.

Intense Hall-current layers were found adjacent to the field-aligned currents. Three types of ion distributions in the Hall-currents were found: (1) nearly magnetized ions moving slightly slower than the ExB drift, (2) a mixture of magnetized cold ions and unmagnetized hot ions, (3) Unmagnetized hot-ion distributions. The most intense Hall-current, flowing dusk to dawn, was associated with the type (3) that took place at the inner edge of an upward FAC

layer associated with the front of the hot Earthward streaming ions, possibly associated with the front of the reconnection jet. The largest Hall-electric field observed during the entire interval was about twice as large as the maximum convection electric field.

These observations showed that field aligned currents in the flow braking region are multi-scale processes involving processes relevant to reconnection jet from thin current sheet and the evolution of the localized flow vortices. The mixing of the hot ions streaming Earthward from the reconnection jet and the tailward moving cold ion components affects the Hall current processes near the dipolarization front. It is important to take into account these multi-scale multi-component plasma processes to understand the evolution of the substorm current wedge.

Acknowledgments

We thank M. Andriopoulou, Y. Narita, E. Panov, D. Schmid, K. Torkar, Z. Vörös, for helping the data analysis and their helpful comments. The authors thank I.R. Mann, D.K. Milling, the CARISMA team (http://www.carisma.ca/), GIMA team (http://magnet.asf.alaska.edu/). The Space Physics Environment Data Analysis Software (SPEDAS, spedas.org) was used for the data processing. We thank the SPEDAS team for their help in using SPEDAS. This work was supported by the Austrian Science Fund (FWF):I2016-N20. JB was supported by NASA under grants NNX13AD10G, NNX13AD21G and by the NSF under grants 1203711 and 160265. VAS, SA, and AP are supported by RSF grant 18-47-05001. MMS, GOES, Geotail data are available from https://lasp.colorado.edu/mms/sdc/, http://satdat.ngdc.noaa.gov, and https://darts.isas.jaxa.jp/stp/geotail/data.html respectively. High-latitude ground-based magnetometer data are retrieved from http://themis.ssl.berkeley.edu/index.shtml. MHD simulations were performed at Los Alamos National Laboratory and the simulation data are available upon request to jbirn@spacescience.org.

References

Birn, J., and M. Hesse (1996), Details of current disruption and diversion in simulations of magnetotail dynamics, J. Geophys. Res., 101, A7, 15345-15358.

Birn, J., R. Nakamura, E. Panov, M. Hesse, Bursty bulk flows and dipolarization in MHD simulations of magnetotail reconnection. J. Geophys. Res. 116, 01210 (2011). doi:10.1029/2010JA016083

Birn, J., M. Hesse, R. Nakamura, and S. Zaharia (2013), Particle acceleration in dipolarization events, J. Geophys. Res., 118, 1960–1971, doi:10.1002/jgra.50132.

Birn, J. and M. Hesse (2014), The substorm current wedge: further insights from MHD simulations. J. Geophys. Res., 119.

Blake, J. B., et al. (2016), The fly's eye energetic particle spectrometer (FEEPS) sensor for the Magnetospheric Multiscale (MMS), Space Sci. Rev., 199, 300–329, doi:10.1007/s11214-015-0163-x.

Chanteur, G., and C. C. Harvey (1998), Spatial interpolation for four spacecraft: Application to magnetic gradients, in Analysis Methods for Multispacecraft Data, edited by G. Paschmann and P. Daly, pp. 349– 369, Eur. Space Agency, Noordwijk, Netherlands.

Egedal, J., W. Daughton, A. Le (2012), Large-scale electron acceleration by parallel electric fields during magnetic reconnection, Nature Physics 8, 321–324, doi:10.1038/nphys2249.

Ergun, R. E., et al. (2016), Magnetospheric Multiscale observations of large-amplitude, parallel, electrostatic waves associated with magnetic reconnection at the magnetopause, Geophys. Res. Lett., 43, 5626–5634, doi:10.1002/2016GL068992.

Fu, H. S., Y. V. Khotyaintsev, M. André, and A. Vaivads (2011), Fermi and betatron acceleration of suprathermal electrons behind dipolarization fronts, Geophys. Res. Lett., 38, L16104, doi:10.1029/2011GL048528.

Fujimoto, K. (2014), Wave activities in separatrix regions of magnetic reconnection, Geophys. Res. Lett., 41, 2721–2728, doi:10.1002/2014GL059893.

Fujimoto, K., and M. Takamoto (2016), Ion and electron dynamics generating the Hall current in the exhaust far downstream of the reconnection x-line, Physics of Plasmas 23, 012903 (2016); doi: 10.1063/1.4940322.

Henderson, MG, G.D. Reeves, J.S. Murphree (1998), Are north-south aligned auroral structures an ionospheric manifestation of bursty bulk flows? Geophys. Res. Lett. 25, 3737.

Higashimori, K., and M. Hoshino (2012), The relation between ion temperature anisotropy and formation of slow shocks in collisionless magnetic reconnection, J. Geophys. Res., 117, A01220, doi:10.1029/2011JA016817.

Hoshino, M., T. Mukai, T. Terasawa. and I. Shinohara (2001), Suprathermal electron acceleration in magnetic reconnection, J. Geophys. Res., 106, A11, 25979-25997.

Kepko, L. et al. (2015), Substorm Current Wedge Revisited, Space Sci Rev (2015) 190:1–46, DOI 10.1007/s11214-014-0124-9.

Kokubun, S. et al., (1994), The GEOTAIL magnetic field experiment, J. Geomag. Geoelectr., 46, 7.

Le Contel, O., et al. (2017), Lower-hybrid drift waves and electromagnetic electron space-phase holes associated with dipolarization fronts and field-aligned currents observed by the Magnetospheric Multiscale mission during a substorm, J. Geophys. Res., 122, doi:10.1002/2017JA024550.

Lindqvist, P.-A., et al. (2016), The spin-plane double probe electric field instrument for MMS, Space Sci. Rev., 199, 137–165, doi:10.1007/s11214-014-0116-9.

Liu, J., V. Angelopoulos, A. Runov, and X.-Z. Zhou (2013), On the current sheets surrounding dipolarizing fluxbundles in the magnetotail: The case for wedgelets, J. Geophys. Res. Space Physics, 118, 2000–2020, doi: 10.1002/jgra.50092.

Liu, J., V. Angelopoulos, X.-Z. Zhou, and A. Runov (2014), Magnetic flux transport by dipolarizing flux bundles, J. Geophys. Res. Space Physics, 119, doi:10.1002/ 2013JA019395.

Lui, A. T. Y. (2013), Cross-tail current evolution during substorm dipolarization, Ann. Geophys., 31, 1131–1142, doi:10.5194/angeo-31-1131-2013.

Mauk, B. H., et al., (2014), The Energetic Particle Detector (EPD) Investigation and the Energetic Ion Spectrometer (EIS) for the Magnetospheric Multiscale (MMS) Mission, Space Sci. Rev., doi:10.1007/s11214-014-0055-5.

McPherron, R.L., C.T. Russell, M.P. Aubry (1973), Satellite studies of magnetospheric substorms on August 15, 1968. 9. Phenomenological model for substorms. J. Geophys. Res. 78, 3131.

Moore, T. E., and J. L. Horwitz (2007), Stellar ablation of planetary atmospheres, Rev. Geophys., 45, RG3002, doi:10.1029/ 2005RG000194.

Nakamura, M. S., M. Fujimoto, and K. Maezawa (1998), Ion dynamics and resultant velocity space distributions in the course of magnetic reconnec-tion, J. Geophys. Res., 103, 4531.

Nakamura, R., W. Baumjohann, R. Schödel, M. Brittnacher, V.A. Sergeev, M. Kubyshkina, T.Mukai, K. Liou (2001), Earthward flow bursts, auroral streamers, and small expansions. J. Geophys. Res. 106, 10791

Nakamura, R., et al., (2009), Evolution of dipolarization in the near-Earth current sheet induced by Earthward rapid flux transport, Ann. Geophys., 27, 1743–1754.

Nakamura, R., et al., (2017), Near-Earth plasma sheet boundary dynamics during substorm dipolarization. Earth, Planets and Space, 69:129, doi:10.1186/s40623-017-0707-2.

Nakamura, T. K. M., R. Nakamura, A. Alexandrova, Y. Kubota, and T. Nagai (2012), Hall magnetohydrodynamic effects for three-dimensional magnetic reconnection with finite width along the direction of the current, J. Geophys. Res., 117, A03220, doi:10.1029/2011JA017006.

Palin, L., et al. (2015), Three-dimensional current systems and ionospheric effects associated with small dipolarization fronts, J. Geophys. Res. Space Physics, 120, 3739–3757, doi:10.1002/2015JA021040

Panov, E. V., et al., (2013), Ionospheric response to oscillatory flow braking in the magnetotail, J. Geophys. Res. Space Physics, 118, 1529–1544, doi:10.1002/jgra.50190.

Pollock, J. C., et al. (2016), (FPI) for the Magnetospheric Multiscale (MMS) Mission, Space Sci. Rev., doi:10.1007/s11214-016-0245-4.

Runov, A., V. Angelopoulos, C. Gabrielse, X.-Z. Zhou, D. Turner, and F. Plaschke (2013), Electron fluxes and pitch-angle distributions at dipolarization fronts: THEMIS multipoint observations, J. Geophys. Res. Space Physics, 118, 744–755, doi:10.1002/jgra.50121.

Russell, C. T., et al., (2016), The Magnetospheric Multiscale Magnetometers, Space Sci. Rev., doi:10.1007/s11214-014-0057-3.

Sauvaud, J.-A., et al. (2004), Case studies of the dynamics of ionospheric ions in the Earth's magnetotail, J. Geophys. Res., 109, A01212, doi:10.1029/2003JA009996.

Schmid, D., et al. (2016), A comparative study of dipolarization fronts at MMS and Cluster, Geophys. Res. Lett., 43, 6012–6019, doi:10.1002/2016GL069520.

Schödel, R., R. Nakamura, W. Baumjohann (2001), T. Mukai, Rapid flux transport and plasma sheet reconfiguration, J. Geophys. Res. 106, 8381.

Schwartz, S. (1998), Shock and discontinuity normal, mach numbers, and related parameters, in Analysis Methods for Multispacecraft Data, edited by G. Paschmann and P. Daly, pp. 249– 270, Eur. Space Agency, Noordwijk, Netherlands.

Sergeev, V. A., V. Angelopoulos, and R. Nakamura (2012), Recent advances in understanding substorm dynamics, Geophys. Res. Lett., 39, L05101, doi:10.1029/2012GL050859

Singer, H., L. Matheson, R. Grubb, A. Newman, and S. Bouwer (1996), Monitoring space weather with the GOES magnetometers, in GOES-8 and Beyond, vol. 2812, edited by E. R. Washwell, pp. 299–308, SPIE Conf. Proc.

Tsyganenko, N. A. (1989), A magnetospheric magnetic field model with a warped tail current sheet, Planet. Space Sci., 37, 5–20, doi:10.1016/0032-0633(89)90066-4.

Tu, J.-N et al. (2000), Statistical nature of impulsive electric fields associatedw ith fast ion flow in the near-Earth plasma sheet, J. Geophy. Res., 105, A8, 1 8,901-18,907.

Wygant, J. R., et al. (2000), Polar spacecraft based comparisons of intense electric fields and Poynting flux near and within the plasma sheet-tail lobe boundary to UVI images: An energy source for the aurora, J. Geophys. Res., 105, 18,675, doi: 10.1029/1999JA900500.

Young, D. T., et al., (2014), Hot Plasma Composition Analyzer for the Magnetospheric Multiscale Mission, Space Sci. Rev., doi:10.1007/s11214-014-0119-6.

Zhou, X.-Z., V. Angelopoulos, A. Runov, J. Liu, and Y. S. Ge (2012), Emergence of the active magnetotail plasma sheet boundary from transient, localized ion acceleration, J. Geophys. Res., 117, A10216, doi:10.1029/2012JA018171.